Improved oxidation behavior of M–20Cr–20Ta (M: Fe, Ni, Co) ternary alloys by formation of complex Cr–Ta-based oxides

Chongchong Tang*, Björn Schäfer, Carsten Schroer, Bronislava Gorr

Institute for Applied Materials (IAM-AWP), Karlsruhe Institute of Technology (KIT), D-76021 Karlsruhe, Germany

*Corresponding author: Chongchong.tang@kit.edu

Abstract

The oxidation behavior and microstructural evolution of M–20Cr–20Ta (M: Ni, Fe, Co) alloys are investigated at 1000°C and 1200°C in Ar–20 vol.% O_2. High-temperature oxidation results in growth of bi-layered oxide scales, featuring an outer Cr_2O_3 layer and an inner Cr–Ta oxide layer. The Cr–Ta oxide layer consists of two distinct phases: $CrTaO_4$ and $CrTa_2O_6$. Significant improvements in oxidation resistance are found for Co and Fe alloys, in consequence of formation of the Cr–Ta oxides. At 1200°C, oxidation kinetics approach a cubic growth law after an initial transient stage, underscoring the exceptional protective capabilities of the Cr–Ta oxides.

Key words: ternary alloys; high-temperature oxidation; $CrTaO_4$ and $CrTa_2O_6$; oxidation kinetics; microstructural evolution

1. Introduction

Tantalum (Ta) is a refractory metal known for its exceptionally high melting point of 2996°C and excellent ductility. Its ability to tolerate interstitial elements (for instance O and N) makes it an appealing choice for application as an alloying element in various alloys. A substantial portion of Ta consumed is utilized as a high-temperature strengthening additive in superalloys [1]. Despite ongoing debate, alloying with Ta has also been frequently reported to enhance the high-temperature oxidation resistance of various types of alloys such as TiAl [2,3], Ni or Co-based (super)alloys [4–7], and Nb–Si-based alloys [8]. For instance, high-temperature oxidation studies on Ni-10Cr alloys show that Ta additions (5 at.%) are particularly beneficial to oxidation resistance in contrast to alloying elements such as tungsten (W), molybdenum (Mo), titanium (Ti), or niobium (Nb) [6]. Ta has positive effects in both isothermal and cyclic oxidation tests, with oxide scales remaining adherent regardless of cycling frequency. Wang et al. report that small addition of Ta (0.5 and 1 wt.%) effectively inhibits NiO formation and reduces the oxidation rate of Ni-16Cr alloys at 1000°C [7]. The beneficial effect of Ta alloying has been attributed to factors such as reduced oxygen solubility within the alloy matrix [3], hindered outward diffusion of cations [4,6], and/or diminished vacancy concentrations in the oxide scale [2,8].

The oxidation behavior of alloys with high Ta concentration has rarely been reported so far. One exception represents Refractory High Entropy Alloys (RHEA) that often contain significant amounts of Ta [9,10]. Some RHEA exhibit high oxidation resistance resulting from the formation of complex $CrTaO_4$-based oxide [11–14]. In the following, key findings of previous work are summarized, highlighting the benefits (+) and drawbacks (-) of this complex oxide:

+ Generally higher thermodynamic stability of $CrTaO_4$ with ΔG_0= -535kJ/molO_2 in comparison to Cr_2O_3 with ΔG_0 = -505 kJ/mol at 1200°C [12];

+ Actually forms in a wide temperature range [11];

+ Growth rate lies between chromia and alumina [11];

+ Excellent adherence of oxide layers to the metallic substrate [11];

+ High solubility of other elements, such as Ti without deterioration of protective properties [12];

+ Inward growth by oxygen diffusion, implicating that break-away oxidation as a result of Cr depletion cannot be expected [12,15];

- Permeable for oxygen and nitrogen, resulting in pronounced internal oxidation and nitridation, respectively [13,15].

Commercial Cr_2O_3-forming high Cr-containing (~15 at.% and above) Fe-, Ni-, and Co-based alloys have been widely used in various high-temperature environments [16]. However, their functionality is significantly challenged at temperatures exceeding 900°C due to the diminished protective properties of the Cr_2O_3 scale, characterized by its accelerated growth rate, increased volatility, and susceptibility to breakdown [17–19]. Alloying with Ta to promote the growth of $CrTaO_4$-based oxides in these alloys offer a promising approach to enhance their high-temperature oxidation resistance and presumably mechanical properties. For instance, Ren et al. reported the improved oxidation resistance of directionally solidified Ni-based alloy by the formation of a continuous $CrTaO_4$ scale [20]. The idea to protect Co-based alloys by $CrTaO_4$ was realized only recently [21]. In the so far published literature, following relevant properties of $CrTaO_4$ were reported [22,23]:

a) The thermal expansion coefficient (TEC) is $6.3x10^{-6}$ K^{-1} which is identical to that of pure Ta;

b) High thermal stability with no structure transformation in the temperature range between 25°C and 1200°C; the melting point is1830 ± 20°C;

c) In terms of the mechanical properties, $CrTaO_4$ belongs to damage tolerant ceramic;

d) The thermal conductivity (k=0.66 $W \cdot m^{-1} \cdot K^{-1}$ at 1000 °C) is much lower than that of currently well-known thermal barrier materials, e.g., yttria stabilized zirconia.

Despite these promising findings, the available research on the properties of $CrTaO_4$ remains limited, with most high-temperature oxidation studies focusing on the addition of Ta in small concentrations. Moreover, a comprehensive comparative study on the effects of Ta alloying across different alloy systems is still lacking. This study investigates the impact of high Ta addition on the phase formation, microstructure, and high-temperature oxidation behavior of traditional high Cr-containing alloys. Three ternary model alloys, Ni–20Cr–20Ta, Fe–20Cr–20Ta, and Co–20Cr–20Ta (at.%), were prepared to explore the effects of Ta at a concentration comparable to $CrTaO_4$-forming TaMoCrTiAl RHEA [19], aiming at promoting growth of the $CrTaO_4$ layer. The alloy constitution and microstructure were analysed before oxidation through a combination of experimental techniques and thermodynamic calculations. To eliminate the effects of nitrogen and better elucidate the scale growth mechanisms, oxidation tests were conducted in Ar–20 vol.% O_2 atmosphere at 1000°C and 1200°C. The evolution of

alloy microstructure, oxidation kinetics and growth mechanisms of oxide scales are thoroughly analyzed and discussed, drawing from microstructural examinations, thermogravimetric analysis, and detailed investigations of the oxide scale compositions. Understanding the microstructural evolution and oxidation behavior of these ternary alloys will provide valuable insights into the design and development of new Ta-containing high-temperature alloys capable of withstanding extreme oxidative environments.

2. Experimental procedures

The three ternary alloys, denoted as Ni20Cr20Ta, Fe20Cr20Ta, and Co20Cr20Ta hereinafter, were prepared using arc melting (Edmund Bühler GmbH) under an argon atmosphere of 0.6 atm. High-purity elemental pellets (≥99.9% purity) were used as raw materials. To ensure alloy homogeneity, the prepared buttons were inverted and remelted at least five times in a water-cooled copper mold. Subsequently, the alloys were homogenized at 1200°C for 24 hours in a flowing argon atmosphere using a high-temperature furnace (Nabertherm GmbH) with heating and cooling rates of 100 °C/h. This homogenization process aimed to dissolve the dendritic microstructure and establish a near-equilibrium microstructure representative of operating conditions. Coupons with approximate dimensions of 5 × 5 × 2 mm were sectioned from the homogenized buttons and then ground with SiC paper up to 2500 grit. Ultrasonic cleaning in ethanol was performed prior to high-temperature oxidation testing to remove surface contaminants.

Isothermal oxidation tests were conducted using a NETZSCH STA 449 F3 Jupiter simultaneous thermal analyser (STA) at 1000°C and 1200°C in an Ar–20 vol.% O_2 environment for 24 h. In the case of Fe20Cr20Ta, further oxidation tests were performed at 1000°C for 12 and 48 h using the same facility. Samples were heated in a flowing argon atmosphere from room temperature to the desired test temperature at a heating rate of 25 K/min. Upon reaching the target temperature, the system was stabilized for a period of 10 min to ensure uniform temperature distribution. Subsequently, an Ar–20 vol.% O_2 gas mixture with a flow rate of 100 ml/min was introduced into the reaction chamber to initiate oxidation. After the specified exposure time, the Ar–20 vol.% O_2 flow was terminated, and the samples cooled down to room temperature in a flowing argon atmosphere. The mass change of each specimen during the experiment was continuously monitored using the integrated balance in the STA equipment.

X-ray diffraction (XRD) using a Seifert PAD II diffractometer was employed to determine the phase composition of the alloys in their as-received state and after oxidation. A classical Bragg-Brentano geometry (θ-2θ) with a step size of 0.01° and a scan speed of 1°/min was utilized, employing Cu $K\alpha_1$ radiation (λ = 0.15406 nm). Scanning electron microscopy (SEM, Philips XL30S and JEOL JSM6400) equipped with energy-dispersive X-ray spectroscopy (EDX) was used to examine the surface morphology, cross-sectional structure, and chemical composition of both the unoxidized and oxidized samples. The specimens were embedded in epoxy resin, followed by polishing with SiC paper and diamond suspensions to prepare cross-sections for investigation. The total oxide scale thickness and individual sublayer thicknesses of the oxidized alloys were quantified using backscattered electron (BSE) cross-sectional images analysed with ImageJ software. The average values and standard deviations were calculated based on measurements from at least three images taken at different positions for each sample.

3. Results

3.1 Microstructure and phase constitution

Fig.1 presents the microstructure and phase constitution of the three alloys after homogenization at 1200°C as identified by SEM and XRD, respectively. All three alloys exhibit a dual-phase structure, characterized by a phase with relatively high-volume fraction, appearing brighter in SEM images (marked as Phase A), and another minor phase (marked as Phase B). The bright Phase A appears as the matrix, whereas Phase B is found primarily at the boundaries of the Phase A domains. The average chemical composition and composition of individual phases measured by EDX are shown in Table 1. The volume fractions of individual phase, estimated using ImageJ software, are also included. In all three alloys, the bright A phases are rich in Ta, while the dark B phases contain higher Cr concentrations.

To better understand the phase equilibria of the corresponding systems, the temperature-dependent volume fractions of different phases were calculated using Thermo-Calc with TCFE7 database. The results are presented in Fig. 2. The calculations predict the formation of a liquid phase and a BCC solid solution (SS) phase of Ni20Cr20Ta at 1200°C, which solidifies into BCC and FCC solid solution phases at slightly lower temperatures. The Fe- and Co-based alloys primarily consist of C14 Laves phase and to a lesser extent of Fe or Co solid solution phases, respectively, at 1200°C. The experimentally observed phase constitutions and their volume fractions are in excellent agreement with the thermodynamic calculations at 1200°C (except for Ni20Cr20Ta), as shown in Table 1 and Fig. 2. The phase constitution observed at room temperature for Ni20Cr20Ta reflects the solidification of the liquid phase upon

cooling. This aligns well with the calculated results at slightly lower temperatures (~1100°C), where the two solid solution phases, Ni_{ss} and Cr_{ss}, are stable, as shown in Fig. 2. However, it should be noted that thermodynamic calculations exhibit some uncertainty in predicting the liquidus temperature of this alloy, as the alloy button retains its shape and displays no evident signs of melting after thermal homogenization at 1200°C (i.e. an underestimation of the liquidus temperature). A significant amount of Ta is dissolved in the Ni_{ss} phase, whereas the Cr_{ss} phase contains predominantly Cr (Cr concentration above 90 at.%). All three alloys maintain their high-temperature phase constitution, with no evidence of the formation of low-temperature stable phases, as illustrated in Fig.1 and Fig. 2.

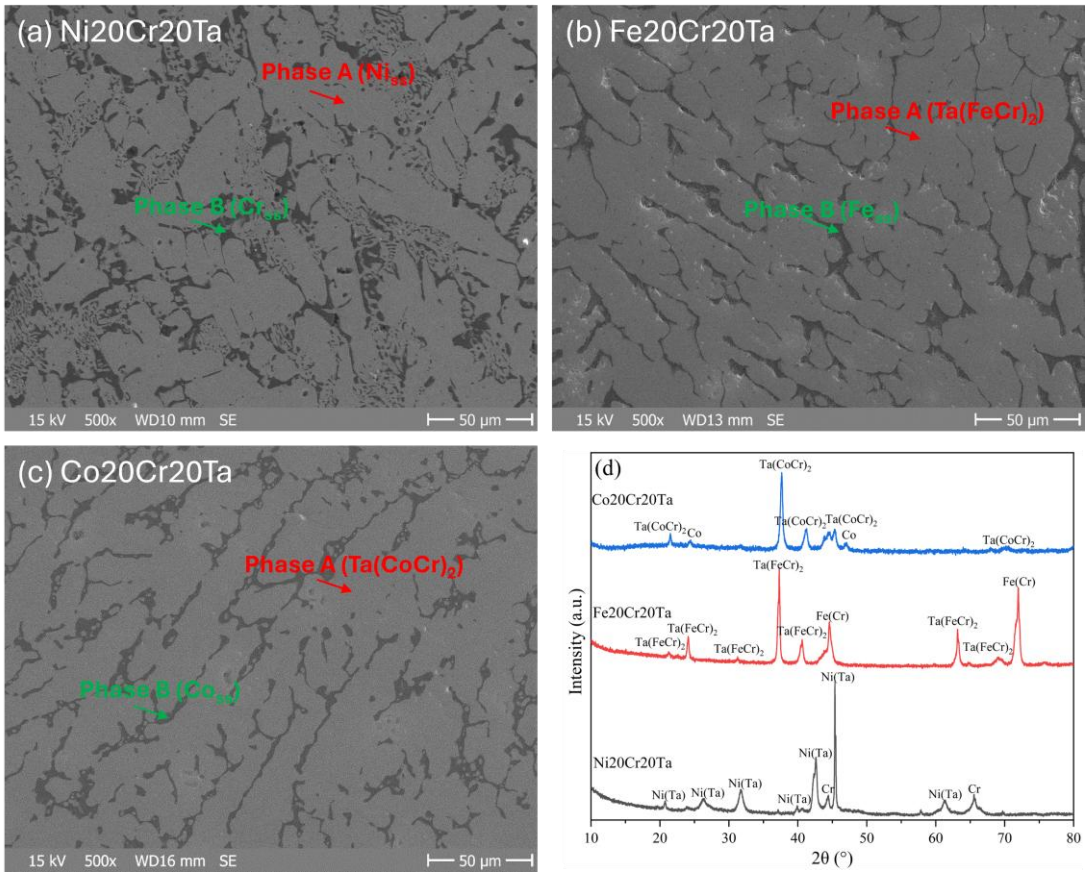

Fig. 1 Microstructure and phase composition of the three alloys after annealing at 1200 °C and cooling to room temperature. The SEM images show the microstructure of (a) Ni20Cr20Ta, (b) Fe20Cr20Ta, (c) Co20Cr20Ta. The XRD patterns are summarized in (d).

Table 1 Chemical composition and volume fraction of the different phases marked in Fig.1

Alloy	Phase	Chemical composition (at%)	Phase identified	Phase fraction (vol.%)
Ni20Cr20Ta	A	Ni: 76.9, Cr: 2.6, Ta: 20.5	Ni_{ss} (FCC_A1)	79.7
	B	Ni: 3.2, Cr: 94.0, Ta: 2.8	Cr_{ss} (BCC_A2)	20.3
	Average	Ni: 58.5, Cr: 21.5, Ta: 20.0	--	--
Fe20Cr20Ta	A	Fe: 50.9, Cr: 14.9, Ta: 34.2	$Ta(FeCr)_2$ (C14)	72.1
	B	Fe: 68.0, Cr: 31.5, Ta: 0.5	Fe_{ss} (BCC_A2)	27.9
	Average	Fe: 55.8, Cr: 21.5 Ta: 22.7	--	--
Co20Cr20Ta	A	Co: 56.6, Cr: 13.4, Ta: 30.0	$Ta(CoCr)_2$ (C14)	68.3
	B	Co: 70.9, Cr: 22.7, Ta: 6.4	Co_{ss} (FCC_A1)	31.7
	Average	Co: 59.2, Cr: 21.3, Ta: 19.5	--	--

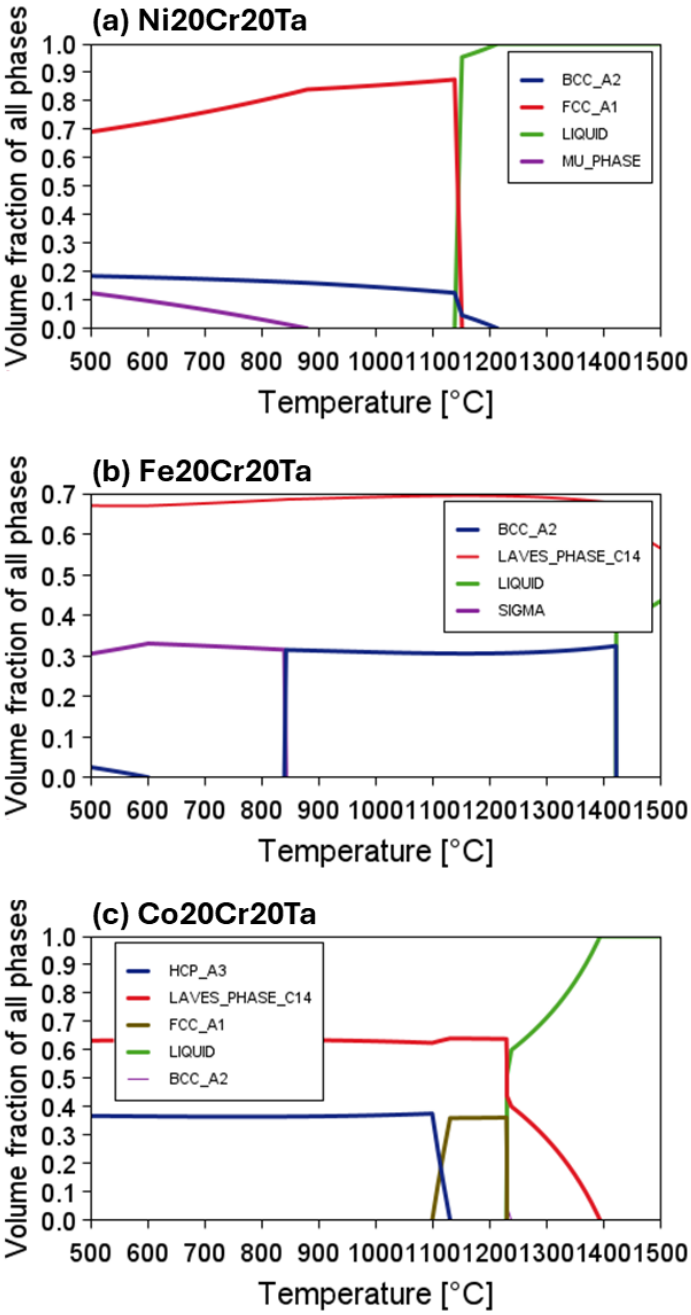

Fig. 2 Volume fraction as a function of temperature of the constituent phase in the three ternary alloys calculated by Thermo-Calc using the TCFE7 database. (a) Ni20Cr20Ta, (b) Fe20Cr20Ta, (c) Co20Cr20Ta.

3.2 High-Temperature Oxidation

3.2.1 Isothermal oxidation kinetics

Fig.3 depicts mass change curves for the three alloys during oxidation at 1000°C and 1200°C for 24 h obtained by thermogravimetry. The solid lines represent the recorded experimental data, while the dashed lines are fitted curves based on the parabolic rate law. The initial application of parabolic rate law enables quantitative comparisons of the oxidation rates between these Ta-containing alloys and their Ta-free counterparts, as well as with commonly protective oxide scales. The good correlation between the experimental data and the parabolic law fitting (except Ni20Cr20Ta at 1200°C) indicates that the oxidation rate decreases over time and the oxidation process is primarily diffusion controlled. The experimental curve recorded for Fe20Cr20Ta at 1000°C deviates somewhat from the fitted curve after 22 h, likely due to disturbance in thermogravimetric balance or edge effects during oxidation. The mass change curve of Ni20Cr20Ta at 1200°C can be more accurately represented by two distinct stages, which correlates with the initially rapid transient oxidation stage, internal oxidation, and void formation (see the subsequent sections). Among all alloys, Ni20Cr20Ta exhibit the highest mass gain, followed by Co20Cr20Ta and Fe20Cr20Ta at both temperatures. Despite the slight variations, the overall mass gains remain relatively low, with all three alloys exhibiting values below 0.8 mg/cm² after 24 h of oxidation at 1000°C. At 1200°C, the final recorded mass gains range from 3.01 mg/cm² to 5.54 mg/cm² for Fe20Cr20Ta and Ni20Cr20Ta, respectively.

Table 2 compares the parabolic rate constants for the three ternary alloys and their respective binary counterparts under similar oxidation conditions (Ar-O_2 or O_2 atmosphere). While the parabolic rate constants for Ni20Cr20Ta are comparable to those of Ni20Cr, Fe20Cr20Ta and Co20Cr20Ta exhibit significantly enhanced oxidation resistance. The parabolic rate constants for Fe20Cr20Ta are one order of magnitude lower, and for Co20Cr20Ta, they are reduced by three orders of magnitude compared to their binary counterparts. These results clearly indicate that addition of 20 at.% Ta substantially enhances the oxidation resistance of the Fe–Cr and Co–Cr systems.

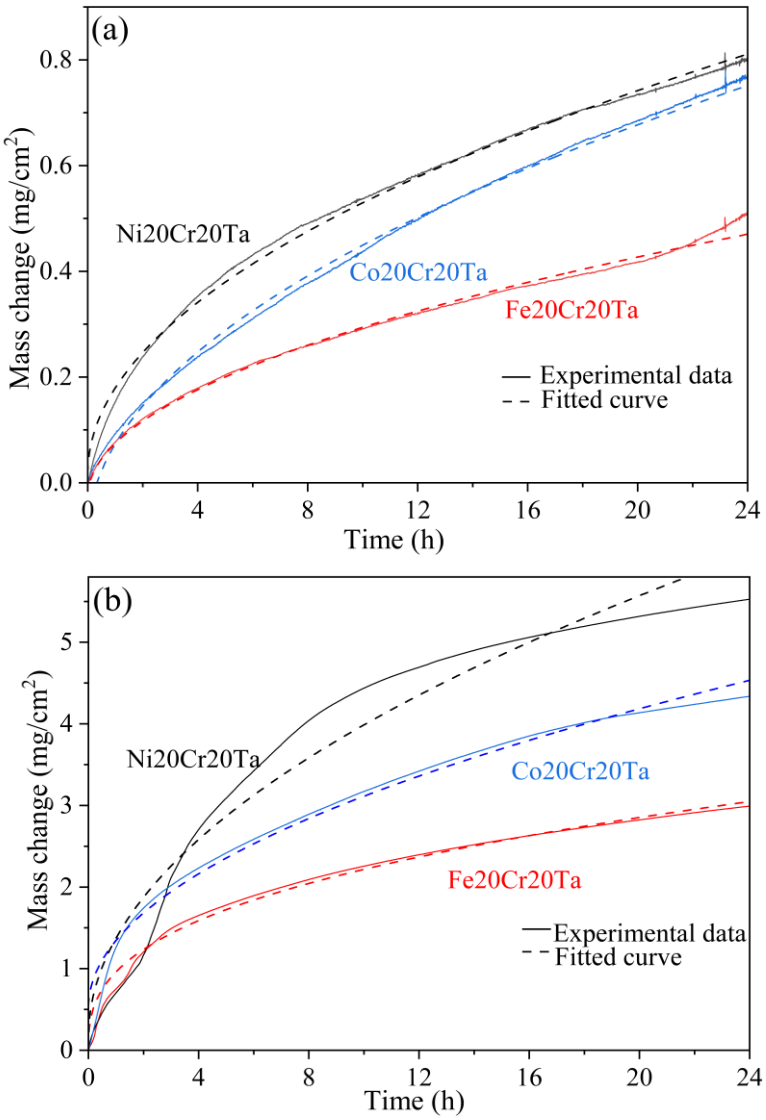

Fig. 3 Mass change curves and fitting results using parabolic law of the three alloys during oxidation at (a) 1000°C and (b) 1200°C for 24 h.

Previous fitting of the mass change curves revealed deviations of their oxidation kinetics from the parabolic law, particularly noticeable at 1200°C for Ni20Cr20Ta. Fig. 4 constructs a double logarithmic plot of mass change versus oxidation time at 1200°C. This plot provides intuitive insight into the oxidation kinetics, with slopes of 1,1/2, and 1/3 corresponding to linear, parabolic, and cubic rate laws, respectively. The analysis reveals two distinct stages in the oxidation process. The initial stage features a more rapid oxidation rate with kinetics between linear and parabolic. As oxidation progresses, the oxidation rate transitions to a slower, steady-state regime, where kinetics approaches a cubic rate law. The transition between these two stages occurs at around 100 min for both Fe20Cr20Ta and Co20Cr20Ta, as indicated by the dashed line in Fig. 4. In contrast, Ni20Cr20Ta exhibits a much longer period before the oxidation rate begins to slow down. The fitted equations for the steady-state regime

oxidation are displayed in Fig.4, with the slope values found to be 0.35, 0.38, and 0.39 for the Fe-, Co-, and Ni-based alloys, respectively. These values are quite close to the ideal cubic law slope of 1/3. A similar analysis of the mass change curves at 1000°C (not shown here) indicates that their oxidation kinetics remain to the parabolic rate law throughout the entire exposure period, which appears to be related to the much lower mass gain here.

Table 2 Parabolic rate constant (K_p: $kg^2 \cdot m^{-4} \cdot s^{-1}$) of the three alloys and comparison with their binary counterparts

Alloy	1000°C	1200°C	Ref.
Ni20Cr	$1.6 \sim 6.9\times10^{-10}$	1.2×10^{-8}	[24–27]
Ni20Cr20Ta	7.4×10^{-10}	4.2×10^{-8}	This study
Fe20Cr	$4.0 \sim 4.8*10^{-9}$	9.5×10^{-8}	[28]
Fe20Cr20Ta	2.8×10^{-10}	8.2×10^{-9}	This study
Co20Cr	$4.1 \sim 4.9\times10^{-7}$	2.7×10^{-5}	[29,30]
Co20Cr20Ta	6.0×10^{-10}	2.6×10^{-8}	This study

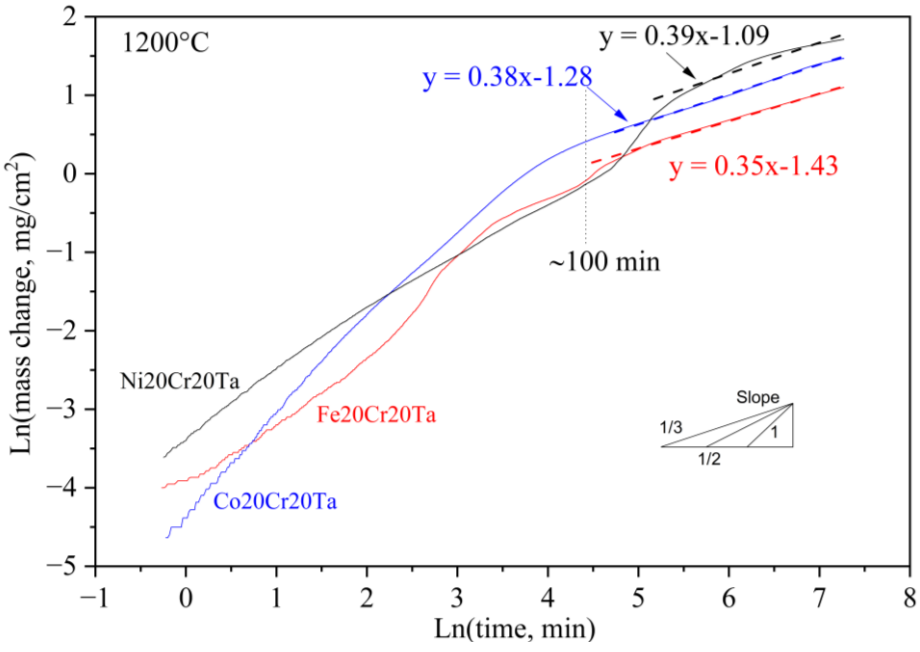

Fig. 4 The double logarithmic graph of the mass change and oxidation time at 1200°C. The oxidation kinetics are closer to cubic law after initial rapid transient oxidation period.

3.2.2 Constituent phases of oxide scales

XRD analyses performed after oxidation for 24 h at 1000 or 1200 °C are shown in Fig. 5. Three distinct oxide phases are identified, aside from the diffraction peaks of the alloy substrate. These phases include binary Cr_2O_3 (PDF No. 38-1479) and two ternary Cr–Ta-based oxide phases, i.e., $CrTaO_4$ (PDF No. 39-1428) and $CrTa_2O_6$ (PDF No. 25-0921). Their theoretical diffraction patterns are also plotted in Fig. 5 for reference. For Ni20Cr20Ta, only signals from Cr_2O_3 and $CrTaO_4$ are clearly present, whereas, for the other two alloys, peaks corresponding to all three oxides are observed. The intensities of oxide peaks are somewhat higher after oxidation at 1200°C as compared to 1000°C. Additionally, the highest intensity peak in spectra recorded from Fe20Cr20Ta or Co20Cr20Ta shifts from Cr_2O_3 at 1000°C to the ternary oxides $CrTa_2O_6$ or $CrTaO_4$, respectively, after oxidation at 1200°C, suggesting the dominance of these ternary oxides within the oxide scale formed at the higher temperature.

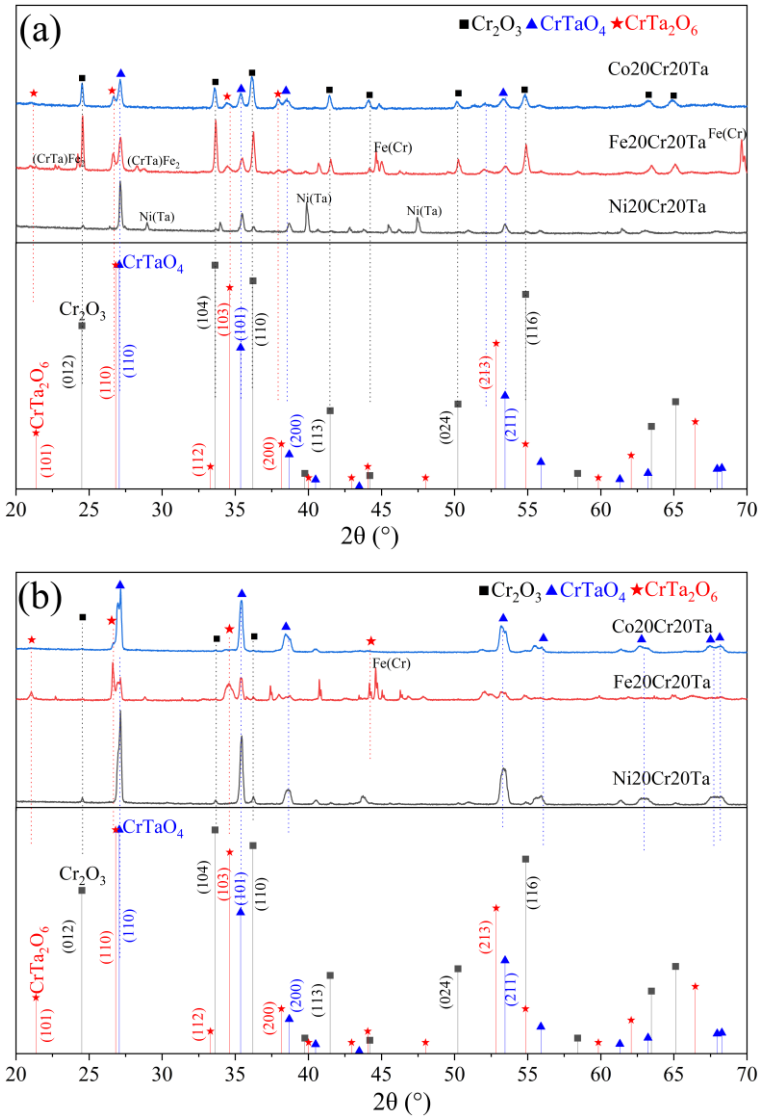

Fig. 5 XRD patterns recorded from the three alloys after oxidation for 24 h and theoretical patterns corresponding to relevant oxides: (a) 1000°C and (b) 1200°C.

3.2.3 Surface morphology and microstructure of oxide scales

The surface morphologies and cross-sectional structures of the oxide scale formed after oxidation at 1000°C are presented in Fig. 6 and Fig.7, respectively. Chemical composition analyses and contrasting morphologies confirm that all three alloys grow a bi-layered oxide scale, consisting of an outer Cr_2O_3 layer and an inner Cr–Ta oxide layer. The outer Cr_2O_3 layer display a convoluted morphology with facetted crystals protruding from the surface, indicative of outward growth at the oxide/gas interface. Spalling of outer Cr_2O_3 scale occurs, whereas the inner Cr–Ta oxide layers seem to remain adherent (Fig.6). Low-magnification SEM images (see Fig.S1) reveals varying degrees of spalling for the three alloys, increasing in the order Co20Cr20Ta < Fe20Cr20Ta < Ni20Cr20Ta. The thermogravimetric curves are inconspicuous as to loss of oxide so that spalling is like to have occurred during cooling after the isothermal exposure, because of thermal stress accumulation when temperature changes [31]. The varying levels of oxide spalling are likely associated with differences in thermal expansion mismatch between alloy matrix and oxide scale, and oxide scale thickness. Although the thermal expansion coefficients of the alloy matrix are not known, the increased thickness of the oxide layer on Ni20Cr20Ta obviously makes the scale more susceptible to spalling (see Fig.7).

The two oxide sublayers exhibit significant thickness variations among the alloys, as quantified in Fig.7 (d). Notably, Ni20Cr20Ta forms a considerably thicker Cr_2O_3 layer and a thinner Cr–Ta oxide layer as compared to the other two alloys (Fig. 7). The average thickness of the Cr_2O_3 layer and the Cr–Ta oxide layer on Ni20Cr20Ta is ~ 6.2 and 0.7 μm, respectively. In comparison, their thicknesses on Co20Cr20Ta average ~ 3.0 and 2.7 μm, respectively. The overall oxide scale thicknesses qualitatively correlate with the mass gains shown in Fig.3 (a). Prominent growth of Cr_2O_3 layer on Ni20Cr20Ta leads to preferential consumption of Cr_{ss} phase beneath the oxide scale, void formation and internal oxidation of Cr on the void surfaces (see Fig.7 (a)). The oxide scales showcase a compact structure with wavy characteristics at both the gas/oxide and oxide/alloy interfaces in Fe20Cr20Ta and Co20Cr20Ta after oxidation. Notably, remnants of the minor solid solution phases are incorporated into the Cr–Ta oxide layer in the form of Fe(Cr) or Co(Cr) particles (see Fig.7 (b) and (c)). In regions where the Cr–Ta oxide layer contains such particles, it exhibits increased thickness and a more convoluted structure. Conversely, particle-free oxide scale is thinner and of uniform thickness. The number density of unoxidized particles is higher within the Cr–Ta oxide layer on Co20Cr20Ta, which likely contributes to the greater variability in its thickness. Elemental mapping (see Fig. S2-4) confirms the formation of bi-layered oxide scales comprising an outer Cr_2O_3 and inner Cr–Ta oxide layer with thicknesses varying across the alloy surface.

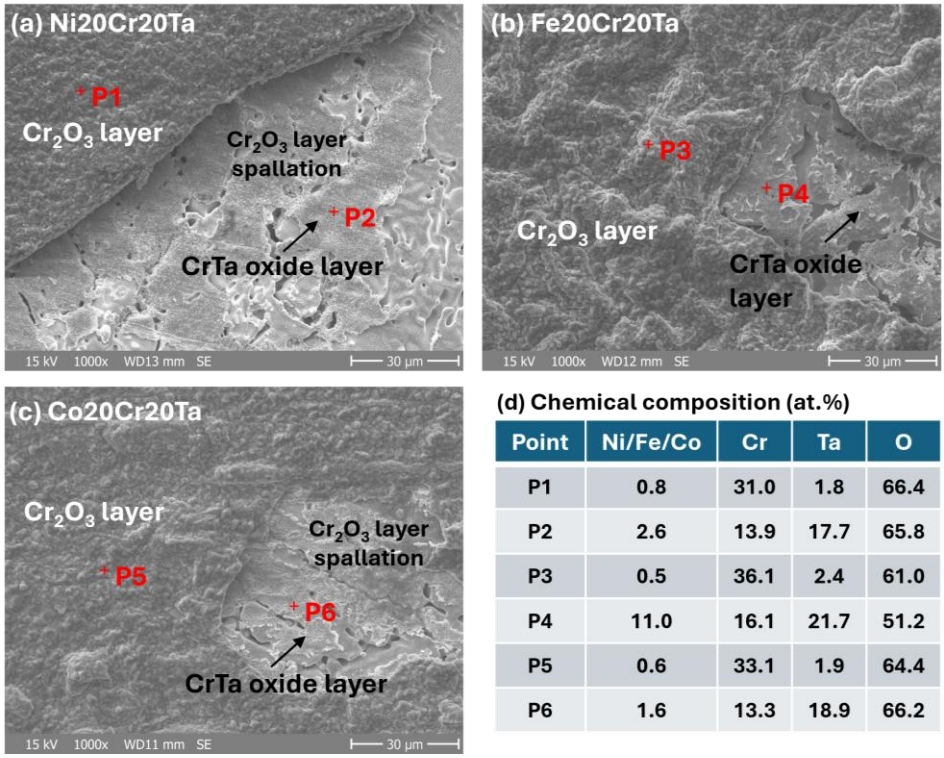

(d) Chemical composition (at.%)

Point	Ni/Fe/Co	Cr	Ta	O
P1	0.8	31.0	1.8	66.4
P2	2.6	13.9	17.7	65.8
P3	0.5	36.1	2.4	61.0
P4	11.0	16.1	21.7	51.2
P5	0.6	33.1	1.9	64.4
P6	1.6	13.3	18.9	66.2

Fig. 6 Surface morphology of the oxide scale after 24 h oxidation at 1000°C for (a) Ni20Cr20Ta, (b) Fe20Cr20Ta, and (c) Co20Cr20Ta. (d) Results of EDS analyses performed at the indicated points.

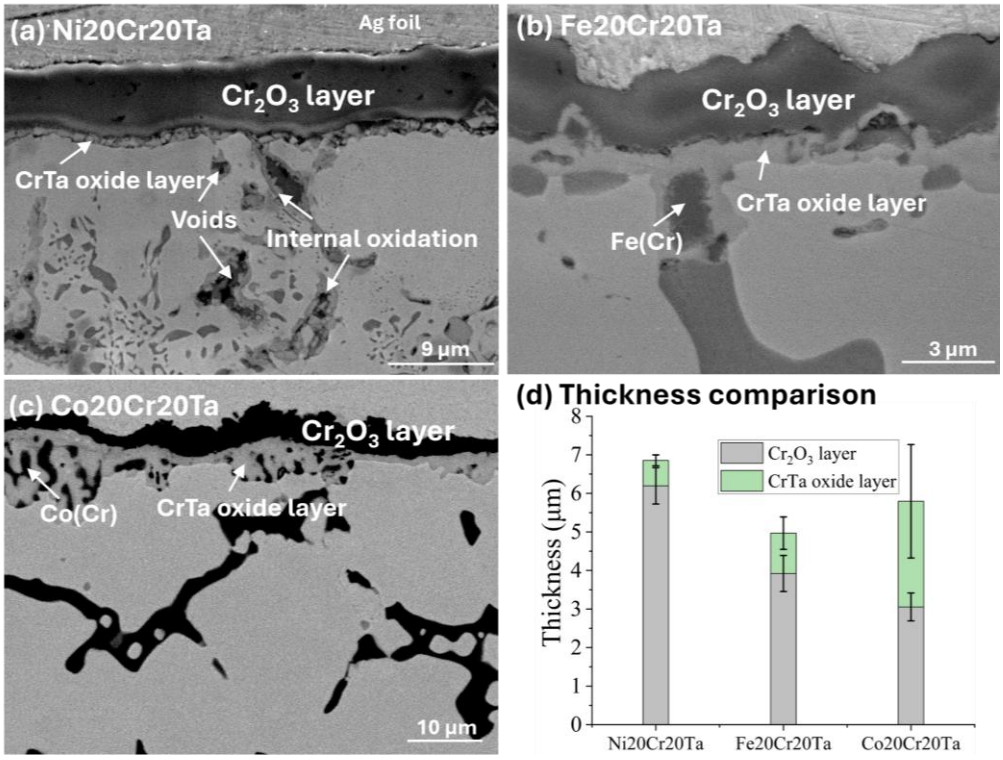

Fig. 7 Cross-sectional morphologies and comparison of their oxide scale thickness after oxidation at 1000°C for 24 h. (a) Ni20Cr20Ta, (b) Fe20Cr20Ta, (c) Co20Cr20Ta. The thicknesses of the two oxide sublayers are summarized in (d). The SEM images are in different magnifications.

Deeper analysis of the oxide scale on Fe20Cr20Ta that formed at 1000 °C, with the aid of EDS line scans (Fig. 8), reveals clear differences in Cr and Ta concentration in the Cr–Ta oxide layer. The Cr concentration is higher in the region adjacent to the Cr_2O_3 layer, transitioning to a Ta-rich zone closer to the oxide/alloy interface. Notably, the Ta:Cr ratio approaches 2 in the oxide surrounding a Fe(Cr) particle and directly above the alloy matrix, suggesting $CrTa_2O_6$, as indicated in the EDS line scan in Fig.8. A qualitatively similar distribution of Cr and Ta is observed for the Cr–Ta oxide layer on Co20Cr20Ta (Fig. S4). These findings, corroborated by the XRD results, reveal the growth of two Cr–Ta-based oxides within the Cr–Ta oxide layer: formation of the $CrTaO_4$ phase beneath the outer Cr_2O_3 layer, and development of the $CrTa_2O_6$ phase under the $CrTaO_4$ and above the alloy matrix.

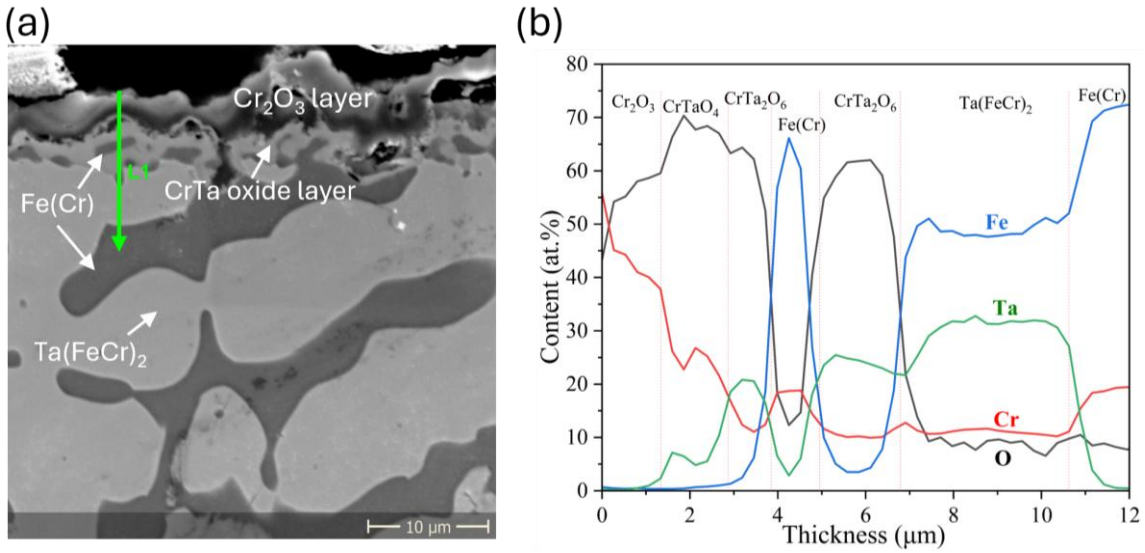

Fig. 8 Cross sectional morphology and EDX line scanning of Fe20Cr20Ta alloy after oxidation at 1000°C for 24 h. (a) SEM image with the position of EDX line scan, and (b) elemental composition profile obtained from the EDX line scan.

The oxide scales formed at 1200°C exhibit similar surface morphologies but with more pronounced spalling of Cr_2O_3 layer as compared to those observed at 1000°C (Fig.S5) because of higher level of thermal stresses and scale thickness [32]. Fig.9 presents cross-sectional views for the three alloys after oxidation at 1200°C as well as EDX point measurements for Ni20Cr20Ta. A bi-layered oxide structure with significantly increased thicknesses, compared to those at 1000°C, is observed in all cases. Similar to the lower temperature, Fe(Cr) or Co(Cr) particles are incorporated into the Cr–Ta oxide layer on Fe20Cr20Ta and Co20Cr20Ta, respectively. Notably, a chemical gradient within the Cr–Ta oxide layer (EDX point measurements P4-P6 in Fig.9 (a)), previously observed only for the Fe- and Co-based alloys, is also detected in the case of the Ni-based alloy now, correlating with the thicker Cr–Ta oxide layer. A pronounced Cr_{ss}-depleted region forms beneath the oxide scale on Ni20Cr20Ta, characterized by a

single Ni_{ss} phase with varying Cr and Ta content. In contrast, Fe20Cr20Ta and Co20Cr20Ta maintain a dual-phase microstructure beneath the oxide scale without significant microstructural changes.

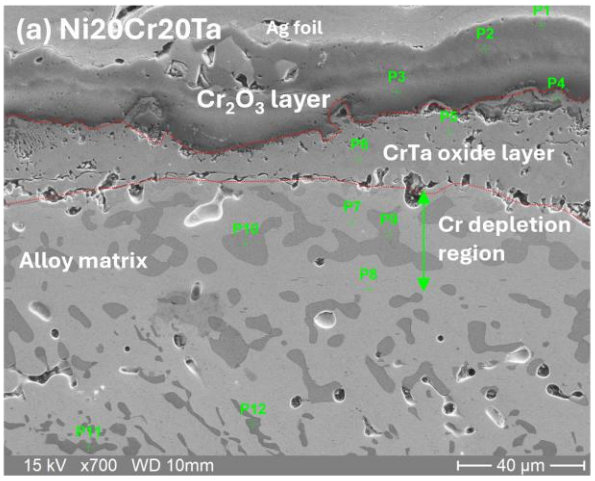

Point	Ni	Cr	Ta	O
P1	0.49	37.72	2.18	59.61
P2	0.56	38.30	2.32	58.82
P3	0.56	35.71	2.39	61.35
P4	1.03	21.77	14.19	63.01
P5	1.39	14.59	19.95	64.07
P6	1.77	14.12	26.15	57.95
P7	76.24	2.82	19.85	1.09
P8	74.90	2.54	19.87	2.68
P9	71.73	14.92	7.47	5.88
P10	72.94	15.86	7.93	3.27
P11	7.71	74.04	2.82	15.43
P12	8.33	74.42	2.74	14.51

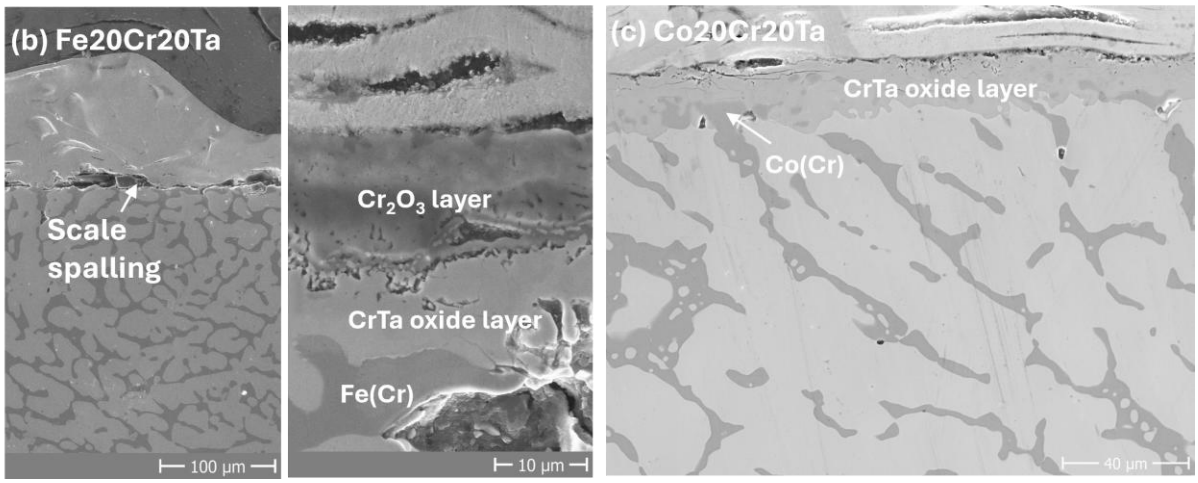

Fig. 9 Cross-sectional morphologies of the three alloys after oxidation at 1200°C for 24 h. (a) Ni20Cr20Ta and EDX point measurements (at.%). The data points in red show the chemical gradient of Cr and Ta within the Cr–Ta oxide layer. (b) Fe20Cr20Ta, and (c) Co20Cr20Ta.

3.2.4 Oxide scale evolution for Fe20Cr20Ta at 1000°C

Fig. 10 illustrates the typical cross-sectional morphologies of the oxide scale and the evolution of oxide layer thicknesses over oxidation time for exposure of 12, 24 and 48 h of Fe20Cr20Ta at 1000 °C. The outer Cr_2O_3 layer exhibits minimal growth, with relatively constant thickness of around 4 μm. In contrast, the inner Cr–Ta oxide layer gradually thickens with exposure time increasing up to 48 h. Given that volatilization of Cr_2O_3 manifests only after prolonged exposure (exceeding ~10 days) at 1000°C

[33], the nearly constant thickness of Cr_2O_3 layer observed here suggests that the formation of the inner Cr–Ta oxide effectively inhibits outward diffusion of Cr.

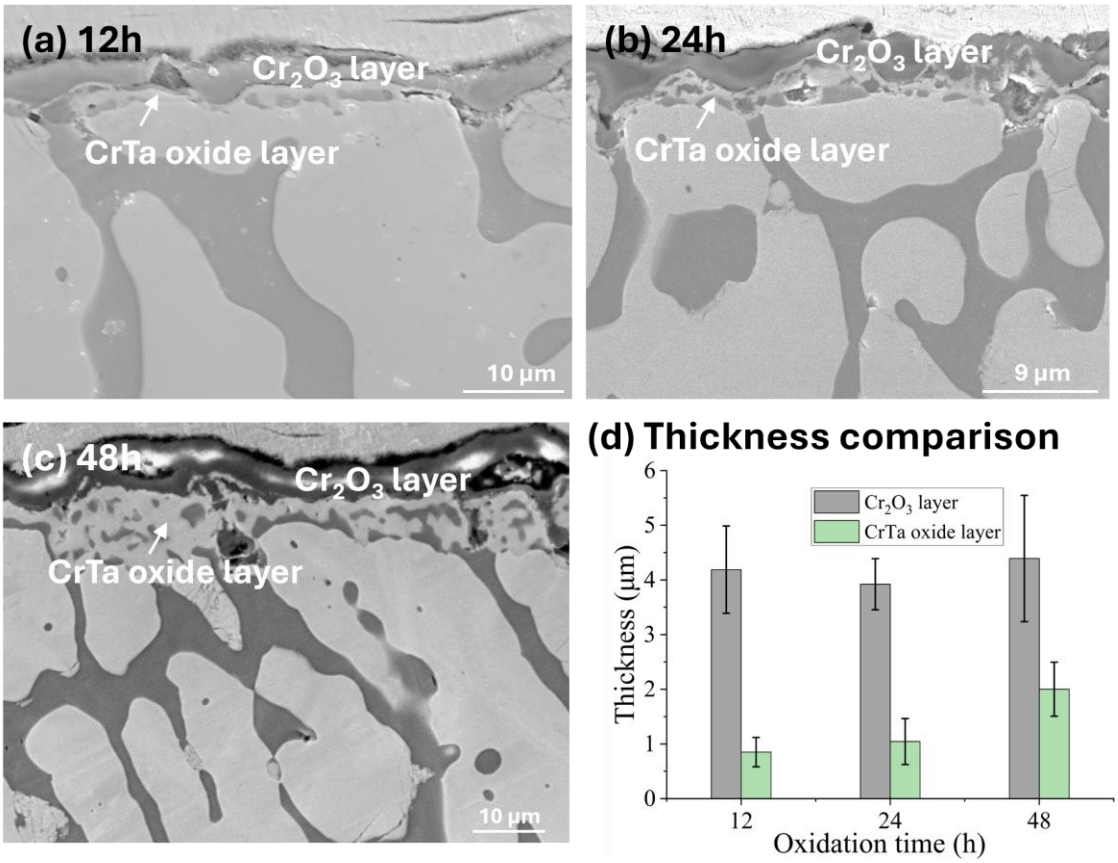

Fig. 10 Cross sectional morphologies of Fe20Cr20Ta after oxidation at 1000°C for three different times (a) 12, (b) 24 and (c) 48 h, and (d) comparison of their oxide scale thickness with the two oxide sublayers. The SEM images are in different magnifications.

4. Discussion

4.1 Oxide formation mechanisms and structural evolution

During oxidation at 1000°C and 1200°C, all three ternary alloys form a bi-layered oxide scale, comprising an external Cr_2O_3 layer and an internal Cr–Ta oxide layer. The formation of such bi-layered oxide scales with varying thickness on each alloy can be rationalized by their phase composition (i.e. chemical activity of alloying elements), thermodynamic stability of resulting oxide phases and diffusion processes. The base elements (Ni, Fe, Co) represent the most noble elements in these ternary alloys, which makes them less susceptible to oxidation at elevated temperatures. At 1200°C, the Gibbs free energy of formation (per mole O_2) for Cr_2O_3 and Ta_2O_5 is approximately -505 kJ/mol and -565 kJ/mol, respectively [34]. These values suggest that both oxides have comparable thermodynamic stability, but with slightly higher stability for Ta_2O_5. Preferential growth of Cr_2O_3 external layers over Ta-containing oxides occurs in all three alloys during oxidation at high temperatures, consistent with observations in TaMoCrTiAl high-entropy alloys containing Cr and Ta in equivalent amounts [34] and recently investigated TaTiCr alloys [35] (excluding the surface layers of TiO_2 and/or Al_2O_3). The initial preferential oxidation of Cr is most likely to be attributed to the higher chemical activity of Cr (see the next paragraph) and sluggish diffusion of Ta atoms within the alloys [35,36].

The observed variation in thickness of the Cr_2O_3 surface layers among the three alloys can be attributed to the differing chemical activities of Cr within the alloys and diffusivity aspects. Using the TCFE7 database, the calculated chemical activities of Cr are 0.00648, 0.00370, and 0.00305 at 1000°C in the Ni, Fe, and Co-based alloys, respectively. In contrast, the chemical activities of Ta are on the order of 10^{-6} for all three alloys. The volume diffusion coefficients of Cr in Ni-based alloys at 1000°C are of the order of 10^{-15} $m^2 \cdot s^{-1}$ [37]. Diffusion data on Laves phases are highly scarce; one study reports that self-diffusivity in Laves phase $NbCo_2$ is approximate 10^{-19} $m^2 \cdot s^{-1}$ at the same temperature [38]. Self-diffusion coefficients in Laves phase $TiFe_2$ also indicate the same magnitude as those in $NbCo_2$ [39]. Therefore, the diffusivity of Cr in Ni20Cr20Ta, which is predominantly composed of solid solution phases, is expected to be significantly faster than that in the Fe and Co alloys where Laves phases dominate. The higher Cr activity and diffusivity in the Ni-based alloy, associated with the presence of solid solution phases, correlates with the formation of a significantly thicker Cr_2O_3 surface layer compared to the Fe and Co-based alloys. The trend in Cr_2O_3 thickness (Fig.7) also corresponds well with the calculated chemical activity values of Cr among the three alloys. Oxidation-induced subsurface microstructural changes are observed in the Ni20Cr20Ta alloy, while no significant phase or microstructural alterations are evident in the other two alloys (Fig. 7 and Fig. 9). In Ni20Cr20Ta, substantial consumption of the

Cr_{ss} phase occurs due to growth of the thicker Cr_2O_3 layer. This leads to the depletion of the Cr_{ss} phase, void formation (Cr outward diffusion), and enrichment of a single Ni_{ss} phase beneath the oxide scale. In contrast, in the Fe- and Co-based alloys, both the solid solution phase and the Laves phase can serve as reservoirs for Cr during oxidation plus growth of thinner external Cr_2O_3 layers, preventing the depletion of either phase.

Regarding the internal oxide layer composed of complex Cr–Ta oxide phases, previous studies [12,15] assume the formation of $CrTaO_4$ phase through a reaction involving Cr_2O_3 and Ta_2O_5 phases as outlined in Equation (1),

$$1/2\ Cr_2O_3\ (s) + 1/2\ Ta_2O_5\ (s) = CrTaO_4\ (s) \quad (1)$$

In the present study, we observed an additional complex ternary oxide, $CrTa_2O_6$, alongside $CrTaO_4$. Fig. 11 illustrates the crystal structures of both oxides. $CrTaO_4$ exhibits a typical rutile structure with random Cr and Ta distribution, whereas $CrTa_2O_6$ possesses an ordered tri-rutile structure with defined cation sites and Cr ions of +2 charge. The formation of $CrTa_2O_6$ can be represented by Equation (2), which involves reactants previously used for bulk oxide synthesis [40],

$$1/3\ Cr_2O_3\ (s) + Ta_2O_5\ (s) + 1/3\ Cr\ (s) = CrTa_2O_6\ (s) \quad (2)$$

Considering the higher thermodynamic stability of Ta_2O_5 compared to Cr_2O_3, as oxidation progresses and the oxygen partial pressure at the scale/alloy interface decreases, the interfacial conditions will become more favorable for the preferential oxidation of Ta and reduction of Cr^{3+} to Cr^{2+}. A plausible hypothesis is that the sequential growth of $CrTaO_4$ occurs initially, followed by the formation of $CrTa_2O_6$ within the internal Cr–Ta oxide layer (Fig.8 and Fig.9). The stoichiometry of the two ternary oxides clearly reveals that a larger proportion of Ta atoms are being oxidized during the formation of the $CrTa_2O_6$ phase at a later stage of the oxidation process.

However, an alternative pathway for $CrTa_2O_6$ formation involving the reaction of already formed $CrTaO_4$ with Ta atoms and inward diffusing oxygen may also be feasible, as outlined in Equation 3,

$$CrTaO_4\ (s) + Ta\ (s) + O_2\ (g) = CrTa_2O_6\ (s) \quad (3)$$

Given the differing valence states of Cr in $CrTaO_4$ and $CrTa_2O_6$, it is anticipated that charge transfer between Cr and Ta atoms occurs during the formation of $CrTa_2O_6$. However, the precise chemical nature and behavior of these complex oxides, particularly regarding their stability and phase transitions, remain insufficiently understood. Further investigations are required to fully elucidate the

structural and chemical characteristics of $CrTa_2O_6$ and similar ternary oxides, especially under high-temperature conditions.

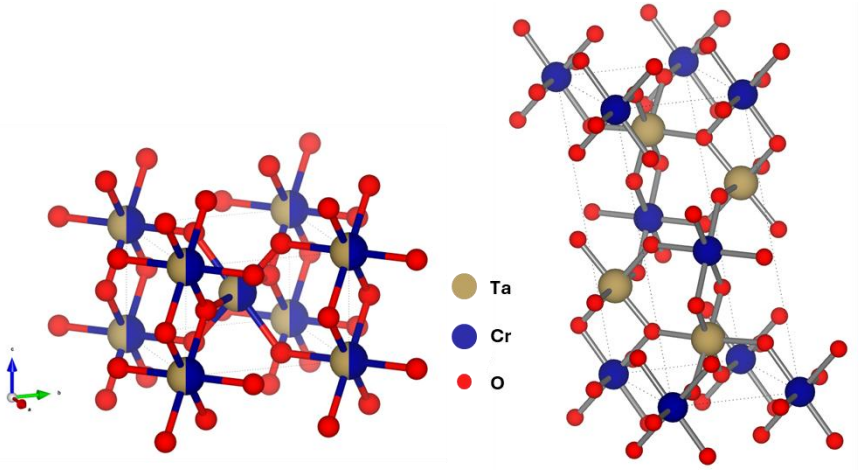

$CrTaO_4$ (rutile structure with random Cr/Ta)	
Crystal structure	Tetragonal (P42nm)
Lattice parameters (Å)	a, b:4.642; c:3.019 α,β,γ:90°
Valence	Cr^{3+}, Ta^{5+}, O^{2-}

$CrTa_2O_6$ (ordered trirutile structure)	
Crystal structure	Monoclinic ($P2_1/n$)
Lattice parameters (Å)	a:4.740, b:4.750, c:9.305 α, γ:90°; β:90.90°
Valence	Cr^{2+}, Ta^{5+}, O^{2-}

Fig. 11 Crystal structure of the two Cr–Ta-based oxides.

4.2 Oxidation kinetics

In Fig.12, the oxidation kinetics fitted using the parabolic rate law for all three alloys (Table 2) are compared with the three most common protective oxide scales (Cr_2O_3, Al_2O_3, and SiO_2) as well as recently reported $CrTaO_4$ scale. Among the three alloys, Fe20Cr20Ta exhibits the slowest oxidation kinetics, with parabolic rate constants aligning closely to the fitting line for the $CrTaO_4$. This appears reasonable since the oxidation resistance of this alloy is primarily governed by the formation of the inner Cr–Ta oxide layer. Previous studies have indicated that the growth of Cr_2O_3 scales is primarily controlled by the outward diffusion of cations [41,42]. The observed minimal change in thickness of the Cr_2O_3 layers in Fe20Cr20Ta alloys after oxidation at 1000°C, despite varying oxidation times (Fig.9), suggests that the dense Cr–Ta oxide layer (consisting of $CrTaO_4$ and $CrTa_2O_6$ here) plays a crucial role in inhibiting the outward diffusion of cations. The growth of Cr–Ta-based oxides further suppress the formation of individual detrimental oxides, i.e. Cr_2O_3 and Ta_2O_5 here, which are known for their poor performance at high temperatures due to volatilization, spalling/cracking. The dense Cr–Ta oxide layer, which grows by inward diffusion of oxygen anions [15,20], explains the low oxidation rate.

However, the parabolic rate constants of the other two alloys, Co20Cr20Ta and, more notably, Ni20Cr20Ta, deviate slightly from the fitting curve for the $CrTaO_4$ scale, with values falling within the region typically associated with the parabolic rate constant of Cr_2O_3 scale. The elevated oxidation kinetics observed in these alloys can be attributed to different factors. For Co20Cr20Ta, a higher density of unoxidized Co(Cr) particles incorporated into the Cr–Ta oxide layer during the oxidation process (as shown in Figs. 7 and 9) likely contributes to the increased oxidation rate. These particles not only increase the roughness of the oxide/alloy interface, thereby enlarging the reactive surface area, but also potentially enhance the solubility and diffusivity of oxygen within the oxide scale compared to the matrix oxide phase. This could lead to more rapid oxidation, slightly deviating from the ideal $CrTaO_4$ behavior. The Ni20Cr20Ta alloys, which exhibit the highest oxidation rate among the three alloys, likely experiences this due to the formation of the thinnest Cr–Ta oxide layer, coupled with void formation and internal oxidation beneath the oxide scale (Fig.8). The thinnest Cr–Ta oxide layer in Ni20Cr20Ta is less effective at impeding the diffusivity of oxidizing species, leading to a higher overall oxidation rate.

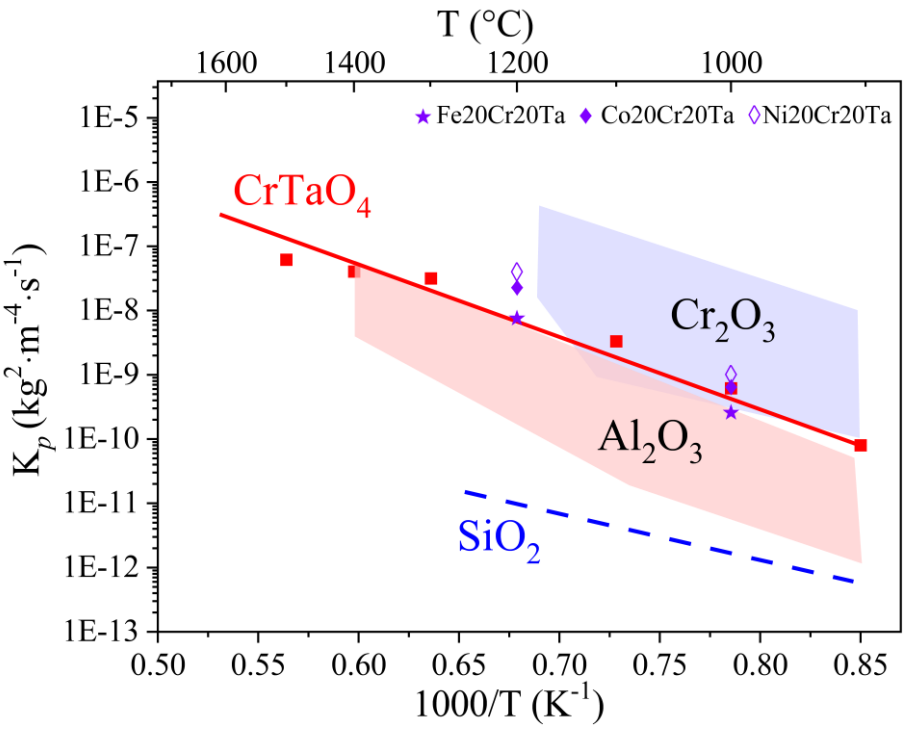

Fig. 12 Comparison of parabolic oxidation kinetics of the three ternary alloys with those most common oxide scales and $CrTaO_4$ scale. The image is adapted and modified from [10].

High-temperature oxidation of alloys with lower Ta content have reported that Ni20Cr, with the addition of 0.5 to 1.5 at.% Ta, exhibits a mass gain between 4.5 and 6 mg/cm² after oxidation at 1000°C for 24 hours in air [7]. In contrast, the Ni20Cr20Ta alloy investigated here shows a much lower mass

gain of less than 1 mg/cm² after oxidation under the same temperature and time conditions (in Ar–20 vol.% O_2). Similar behavior was observed for Co–Cr alloys, where the mass gain recorded in this study was substantial lower compared to previous studies on alloys with lower Ta content [21,43]. An increase in Ta content suppresses the oxidation of base elements and accelerates the formation of continuous Cr–Ta-based oxide layers, improving oxidation resistance and reducing oxidation kinetics.

Previous double-logarithmic plots of the mass change curves at 1200°C (Fig. 4) reveal two distinct oxidation rate regimes: an initial transient period of rapid oxidation with kinetics between linear and parabolic, and a subsequent steady-state regime characterized by an approximate cubic rate law. The first stage likely corresponds to the growth of the Cr_2O_3 surface layer, while the subsequent stage is characterized by the gradual thickening of the inner Cr–Ta oxide layer, as supported by phase and microstructural observations before. The longer transient stage observed in Ni20Cr20Ta before the onset of slower oxidation rate can be explained by the more substantial growth of the external Cr_2O_3 layer in this specific alloy (Fig.7). A similar phenomenon, where oxidation kinetics transition from the parabolic law to the cubic law, was recently reported after the growth of continuous and dense $CrTaO_4$ layer on Ta-alloyed Ni superalloys [20]. Cubic scale growth rate, where the oxidation rate decreases more rapidly than in parabolic growth, is favorable for oxidation protection and enhances the lifetime of the materials.

The growth of the inner Cr–Ta oxide layer, dominated by the inward diffusion of oxygen, is driven by two primary mechanisms: grain boundary diffusion (D_{gb}) and lattice diffusion (D_l) occurring via oxygen vacancies. The observed kinetics transition to cubic rate law during oxidation is often explained by the phenomenon of grain growth in the oxide scale, which reduces the total grain boundary area available for diffusion [44,45]. Previous studies have identified a relatively thick internal oxidation and nitridation zone beneath the $CrTaO_4$ scale during the high-temperature oxidation of TaMoCrTiAl RHEAs in air [12,15,34]. This phenomenon has been attributed to the high concentration of oxygen vacancies within the $CrTaO_4$ scale. According to classical defect theory, the formation of the $CrTa_2O_6$ phase, which has a higher Ta concentration by substitution of Ta ions (+5) for Cr ions (+3 or +2) on the cationic sublattice compared to $CrTaO_4$, could lead to a reduction in oxygen vacancy concentration [32]. The corresponding defect equation, assuming Cr ions with a +3 charge, can be expressed as:

$$V_O^{\bullet\bullet} + 2\,e' + Ta_2O_5 = 2\,Ta_{Cr}^{\bullet\bullet} + 3\,O_O + \,O_2\,(g)\, + \,4\,e' \qquad (4)$$

This reduction in oxygen vacancies could subsequently decrease the lattice diffusion of oxygen, further diminishing the oxidation rate and enhancing the overall oxidation resistance of the alloys.

4.3 Implications of Ta content

All three ternary alloys with 20 at.% Ta successfully develop an inner, continuous Cr–Ta-based oxide layer during high-temperature oxidation, although with variations in layer thickness. However, it is important to note that hexagonal C14 Laves phases serve as matrix in Fe- and Co-based alloys. While Laves phases show promising mechanical properties at high temperatures, they are inherently brittle at intermediate/low temperatures. Previous studies on various Laves phases have reported their ductile-brittle transition temperatures at or above $0.6T_m$ (melting temperature) [46][47]. Recent studies also have reported diminished ductility with an increasing volume fraction of Laves phases in various HEA systems by tuning alloy compositions [48][49]. Nevertheless, it has been demonstrated that with proper control of precipitation process, Laves phases can effectively serve as strengthening particles within a ductile matrix [47]. The critical Ta content required to form the inner protective Cr–Ta-based oxide layer in these ternary alloy systems has not yet been determined. Previous studies on Ni20Cr [7] and Co20Cr alloys [43] have reported that Ta concentrations below 5 at.% are sufficient to promote the formation of $CrTaO_4$ oxide during high-temperature oxidation; although, in most cases, these oxides exist as isolated particles and discontinuous layers at low Ta concentrations. It can be anticipated that the Ta content can be reduced and optimized in these high-Cr alloys, balancing both mechanical properties and oxidation resistance.

4. Summary and conclusion

This study explores the potential of the formation of Cr–Ta oxides on M-20Cr-20Ta alloys (where M = Ni, Fe, Co) at 1000°C and 1200°C in Ar–20 vol.% O_2. The key findings and their implications are summarized as follows:

- All three alloys exhibit a duplex structure, with Ni-based alloys consisting of Ni_{ss} and Cr_{ss} phases, and Fe- and Co-based alloys featuring a solid solution phase and C14 Laves phase.

- A bi-layered oxide scale, consisting of an external Cr_2O_3 layer and an internal Cr–Ta oxide layer, develops across all three alloys during oxidation at 1000°C and 1200°C. The inner Cr–Ta oxide layer composes of two complex ternary oxides, with $CrTaO_4$ presumably initially forming and subsequently transforming into $CrTa_2O_6$. The distinct phase compositions of the alloys result in varying thickness of the oxide sub-layers, along with subsurface microstructural changes (Cr_{ss} depletion and void formation) in Ni20Cr20Ta after oxidation.

- While Ni20Cr20Ta exhibit a similar oxidation rate to its Ta-free counterpart, significant diminished oxidation rates are observed in Co20Cr20Ta and, particularly, in Fe20Cr20Ta because of the formation

of the protective Cr–Ta-based oxide layer. The oxidation kinetics approach a cubic rate law following an initially rapid transient oxidation stage at 1200°C, emphasizing the exceptional protective properties of the Cr–Ta oxide layer.

- Concluding, this study underscores the remarkable potential of complex Cr–Ta oxides ($CrTaO_4$ and $CrTa_2O_6$) to serve as protective scale, effectively safeguarding alloys from rapid oxidation-induced degradation. These findings offer valuable insights for the design and optimization of Ta-containing traditional high-temperature alloys for applications demanding exceptional oxidation resistance.

Declaration of Competing Interest

The authors declare that they have no known competing financial interests or personal relationships that could have appeared to influence the work reported in this paper.

Data availability

Data will be made available on request.

Acknowledgements

The authors acknowledge the financial support provided by the Deutsche Forschungsgemeinschaft (DFG–German Research Foundation, 524725651).

References

[1] R.W. Buckman, New Applications for Tantalum and Tantalum Alloys, Jom 52 (2000) 40–41.

[2] P.V. Cobbinah, W. Matizamhuka, R. Machaka, M.B. Shongwe, Y. Yamabe-Mitarai, The effect of Ta additions on the oxidation resistance of SPS-produced TiAl alloys, Int. J. Adv. Manuf. Technol. 106 (2020) 3203–3215. https://doi.org/10.1007/s00170-019-04885-7.

[3] D. Vojtěch, T. Popela, J. Kubásek, J. Maixner, P. Novák, Comparison of Nb- and Ta-effectiveness for improvement of the cyclic oxidation resistance of TiAl-based intermetallics, Intermetallics 19 (2011) 493–501. https://doi.org/10.1016/j.intermet.2010.11.025.

[4] S.J. Park, S.M. Seo, Y.S. Yoo, H.W. Jeong, H.J. Jang, Effects of Al and Ta on the high temperature oxidation of Ni-based superalloys, Corros. Sci. 90 (2015) 305–312. https://doi.org/10.1016/j.corsci.2014.10.025.

[5] J.W.X. Wo, M.C. Hardy, H.J. Stone, The Effect of Nb, Ta, and Ti on the Oxidation of a New Polycrystalline Ni-Based Superalloy, High Temp. Corros. Mater. 101 (2024) 485–509. https://doi.org/10.1007/s11085-023-10218-7.

[6] P. Elliott, A.F. Hampton, The influence of ternary additions of W, Mo, Ti, Ta, and Nb on the isothermal and cyclic oxidation of Ni-10Cr alloy, Oxid. Met. 14 (1980) 449–468. https://doi.org/10.1007/BF00603612.

[7] H. Wang, J. Guo, S. Lei, W. Li, X. Zhang, Unveiling the formation of oxide layers on Ni-16Cr and Ni-20Cr alloys by the addition of Ta, J. Alloys Compd. 965 (2023) 171361. https://doi.org/10.1016/j.jallcom.2023.171361.

[8] J. Yu, D. Chen, F. Xu, S. Wang, X. Cui, W. Gong, R. Chen, Simultaneous improving high temperature oxidation resistance and room temperature toughness of Nb–Si based alloy via appropriate Ta content addition strategy, Int. J. Refract. Met. Hard Mater. 124 (2024) 106800. https://doi.org/10.1016/j.ijrmhm.2024.106800.

[9] W. Xiong, A.X.Y. Guo, S. Zhan, C.T. Liu, S.C. Cao, Refractory high-entropy alloys: A focused review of preparation methods and properties, J. Mater. Sci. Technol. 142 (2023) 196–215. https://doi.org/10.1016/j.jmst.2022.08.046.

[10] B. Gorr, S. Schellert, F. Müller, H.J. Christ, A. Kauffmann, M. Heilmaier, Current Status of Research on the Oxidation Behavior of Refractory High Entropy Alloys, Adv. Eng. Mater. 23 (2021) 2001047. https://doi.org/10.1002/adem.202001047.

[11] B. Gorr, F. Müller, S. Schellert, H.J. Christ, H. Chen, A. Kauffmann, M. Heilmaier, A new strategy to intrinsically protect refractory metal based alloys at ultra high temperatures, Corros. Sci. 166 (2020) 108475. https://doi.org/10.1016/j.corsci.2020.108475.

[12] S. Schellert, B. Gorr, S. Laube, A. Kauffmann, M. Heilmaier, H.J. Christ, Oxidation mechanism of refractory high entropy alloys Ta-Mo-Cr-Ti-Al with varying Ta content, Corros. Sci. 192 (2021) 109861. https://doi.org/10.1016/j.corsci.2021.109861.

[13] S. Schellert, B. Gorr, H.J. Christ, C. Pritzel, S. Laube, A. Kauffmann, M. Heilmaier, The Effect of Al on the Formation of a CrTaO4 Layer in Refractory High Entropy Alloys Ta-Mo-Cr-Ti-xAl, Oxid. Met. 96 (2021) 333–345. https://doi.org/10.1007/s11085-021-10046-7.

[14] K.C. Lo, Y.J. Chang, H. Murakami, J.W. Yeh, A.C. Yeh, An oxidation resistant refractory high entropy alloy protected by CrTaO 4 -based oxide, Sci. Rep. 9 (2019) 3–4. https://doi.org/10.1038/s41598-019-43819-x.

[15] F. Müller, B. Gorr, H.J. Christ, J. Müller, B. Butz, H. Chen, A. Kauffmann, M. Heilmaier, On the oxidation mechanism of refractory high entropy alloys, Corros. Sci. 159 (2019) 108161. https://doi.org/10.1016/j.corsci.2019.108161.

[16] N. Birks, G.H. Meier, F.S. Pettit, Introduction to the High Temperature Oxidation of Metals, 2nd ed., Cambridge University Press, 2006.

[17] B. Gleeson, M.A. Harper, The long-term, cyclic-oxidation behavior of selected chromia-forming alloys, Oxid. Met. 49 (1998) 373–399. https://doi.org/10.1023/a:1018874206733.

[18] P. Berthod, Kinetics of high temperature oxidation and chromia volatilization for a binary Ni-Cr alloy, Oxid. Met. 64 (2005) 235–252. https://doi.org/10.1007/s11085-005-6562-8.

[19] T. Cheng, J.R. Keiser, M.P. Brady, K.A. Terrani, B.A. Pint, Oxidation of fuel cladding candidate materials in steam environments at high temperature and pressure, J. Nucl. Mater. 427 (2012) 396–400. https://doi.org/10.1016/j.jnucmat.2012.05.007.

[20] W. Ren, F. Ouyang, B. Ding, Y. Zhong, J. Yu, Z. Ren, L. Zhou, The influence of CrTaO4 layer on the oxidation behavior of a directionally-solidified nickel-based superalloy at 850–900 °C, J. Alloys Compd. 724 (2017) 565–574. https://doi.org/10.1016/j.jallcom.2017.07.066.

[21] M. Louis Etienne, G. Stéphane, L. Guillaume, M. Hideyuki, Microstructure and oxidation behavior of Co–Cr–Ta ternary alloys, J. Alloys Compd. 936 (2023) 167968. https://doi.org/10.1016/j.jallcom.2022.167968.

[22] S. Zhang, X. Wang, C. Zhang, H. Xiang, Y. Li, C. Fang, M. Li, H. Wang, Y. Zhou, Microstructure, elastic/mechanical and thermal properties of CrTaO4: A new thermal barrier material?, J. Adv. Ceram. 13 (2024) 373–387. https://doi.org/10.26599/jac.2024.9220862.

[23] S. Hao, Q.J. Hong, M.C. Gao, A prediction of the thermodynamic, thermophysical, and mechanical properties of CrTaO4 from first principles, J. Am. Ceram. Soc. 106 (2023) 7654–7669. https://doi.org/10.1111/jace.19390.

[24] D. Simon, B. Gorr, H.J. Christ, Effect of Atmosphere and Sample Thickness on Kinetics, Microstructure, and Compressive Stresses of Chromia Scale Grown on Ni–25Cr, Oxid. Met. 87 (2017) 417–429. https://doi.org/10.1007/s11085-016-9702-4.

[25] P.Y. Hou, J. Stringer, Effect of Surface-Applied Reactive Element Oxide on the Oxidation of Binary Alloys Containing Cr, Proc. - Electrochem. Soc. 86–2 (1986) 198–211.

[26] I.G. Wright, B.A. Wilcox, R.I. Jaffee, The high-temperature oxidation of Ni-20%Cr alloys containing various oxide dispersions, Oxid. Met. 9 (1975) 275–305. https://doi.org/10.1007/BF00613277.

[27] D. Simon, B. Gorr, M. Hänsel, V. Shemet, H.J. Christ, W.J. Quadakkers, Effect of in-situ gas changes on thermally grown chromia scales formed on Ni-25Cr alloy at 1000°C in atmospheres with and without water vapour, Mater. High Temp. 32 (2015) 238–247. https://doi.org/10.1179/0960340914Z.000000000108.

[28] E.J. Felten, High-Temperature Oxidation of Fe-Cr Base Alloys with Particular Reference to Fe-Cr-Y Alloys, J. Electrochem. Soc. 108 (1961) 490. https://doi.org/10.1149/1.2428122.

[29] I.G. Wright, G.C. Wood, The isothermal oxidation of Co-Cr alloys in 760 Torr oxygen at 1000°C, Oxid. Met. 11 (1977) 163–191. https://doi.org/10.1007/BF00606542.

[30] G.C. Wood, F.H. Stott, The influence of aluminum additions on the oxidation of Co-Cr alloys at 1000 and 1200°C, Oxid. Met. 3 (1971) 365–398. https://doi.org/10.1007/BF00614630.

[31] A.G. Evans, D.R. Mumm, J.W. Hutchinson, G.H. Meier, F.S. Pettit, Mechanisms controlling the durability of thermal barrier coatings, Prog. Mater. Sci. 46 (2001) 505–553. https://doi.org/10.1016/S0079-6425(00)00020-7.

[32] D.J. Young, High Temperature Oxidation and Corrosion of Metals, Elsevier, 2008. https://doi.org/10.1016/S1875-9491(08)00010-0.

[33] C.S. Tedmon, The Effect of Oxide Volatilization on the Oxidation Kinetics of Cr and Fe-Cr Alloys, J. Electrochem. Soc. 113 (1966) 766. https://doi.org/10.1149/1.2424115.

[34] S. Schellert, M. Weber, H.J. Christ, C. Wiktor, B. Butz, M.C. Galetz, S. Laube, A. Kauffmann, M. Heilmaier, B. Gorr, Formation of rutile (Cr,Ta,Ti)O2 oxides during oxidation of refractory high entropy alloys in Ta-Mo-Cr-Ti-Al system, Corros. Sci. 211 (2023) 110885. https://doi.org/10.1016/j.corsci.2022.110885.

[35] N.J. Welch, M.J. Quintana, S.J. Kuhr, T.M. Butler, P.C. Collins, Intermediate and high-temperature oxidation behavior of an equiatomic TaTiCr RCCA from 800 °C to 1400 °C, Int. J. Refract. Met. Hard Mater. 118 (2024) 106437. https://doi.org/10.1016/j.ijrmhm.2023.106437.

[36] O.N. Senkov, S.L. Semiatin, Microstructure and properties of a refractory high-entropy alloy

after cold working, J. Alloys Compd. 649 (2015) 1110–1123. https://doi.org/10.1016/j.jallcom.2015.07.209.

[37] T.F. Chen, G.P. Tiwari, Y. Iijima, K. Yamauchi, Volume and grain boundary diffusion of chromium in Ni-base Ni-Cr-Fe alloys, Mater. Trans. 44 (2003) 40–46. https://doi.org/10.2320/matertrans.44.40.

[38] H. Martin, H. Helmut, Diffusion in the c15-type intermetallic laves phase NbCo2, Philos. Mag. A 80 (2000) 1245–1263. https://doi.org/10.1080/01418610008212113.

[39] H. Mehrer, Diffusion in Intermetallics, Mater. Trans. JIM 37 (1996) 1259–1280.

[40] V. Guillen-Viallet, J.F. Marucco, M. Ghysel, Synthesis, characterization, electrical and magnetic properties of CrTa2O6 and CrNb2O6, J. Alloys Compd. 317–318 (2001) 127–131. https://doi.org/10.1016/S0925-8388(00)01328-1.

[41] S.C. Tsai, A.M. Huntz, C. Dolin, Growth mechanism of Cr2O3 scales: Oxygen and chromium diffusion, oxidation kinetics and effect of yttrium, Mater. Sci. Eng. A 212 (1996) 6–13. https://doi.org/10.1016/0921-5093(96)10173-8.

[42] T.D. Nguyen, J. Zhang, D.J. Young, Effects of H2 on microstructures of Cr2O3 scales grown in water vapour and consequences for breakaway, Corros. Sci. 236 (2024) 112265. https://doi.org/10.1016/j.corsci.2024.112265.

[43] G.N. Irving, J. Stringer, D.P. Whittle, The oxidation of Co-20% Cr base alloys containing Nb or Ta, Corros. Sci. 15 (1975) 337–344. https://doi.org/10.1016/S0010-938X(75)80015-1.

[44] D.J. Tallman, B. Anasori, M.W. Barsoum, A Critical Review of the Oxidation of Ti2AlC, Ti3AlC2 and Cr2AlC in Air, Mater. Res. Lett. 1 (2013) 115–125. https://doi.org/10.1080/21663831.2013.806364.

[45] N. Zou, Y.P. Zhang, J.H. Xu, X. Wang, M.Y. Wang, M.A. Diop, Oxidation Kinetics in Ni-Cr Alloys Through Comprehensive Analysis of Parabolic and Cubic Grain Growth Dynamics and Their Implications on High-Temperature Oxidative Stability, Jom (2024) 12–14. https://doi.org/10.1007/s11837-024-06773-2.

[46] J.D. Livingston, Laves-Phase Superalloys?, Phys. Status Solidi A 415 (1992) 415–423.

[47] F. Stein, A. Leineweber, Laves phases: a review of their functional and structural applications and an improved fundamental understanding of stability and properties, J. Mater. Sci. 56 (2021) 5321–5427. https://doi.org/10.1007/s10853-020-05509-2.

[48] A.E. Mann, J.W. Newkirk, Compositional Modifications to Alter and Suppress Laves Phases in AlxCrMoTayTi Alloys, Adv. Eng. Mater. 25 (2023) 1–8. https://doi.org/10.1002/adem.202201614.

[49] H. Yi, L. Ni, B. Yin, M. Liang, H. Yang, Y. Yang, Investigation on oxidation behavior and mechanical properties of FeCoNiNbAlCrTa high entropy alloy at 900 °C, J. Mater. Res. Technol. 33 (2024) 9405–9414. https://doi.org/10.1016/j.jmrt.2024.11.250.